Tuning the Formation and Rupture of Single Ligand-Receptor Bonds by Hyaluronan-Induced Repulsion

Philippe Robert,* Kheya Sengupta,† Pierre-Henri Puech,* Pierre Bongrand,* and Laurent Limozin*
*INSERM UMR 600, Centre National de la Recherche Scientifique, and UMR 6212, Université de la Méditerranée, Marseille, France; and †Centre Interdisciplinaire de Nanoscience de Marseille, Centre National de la Recherche Scientifique, UPR 3118, Luminy, Marseille, France

ABSTRACT We used a combination of laminar flow chamber and reflection interference microscopy to study the formation and rupture of single bonds formed between Fc-ICAM-1 attached to a substrate and anti-ICAM-1 carried by micrometric beads in the presence of a repulsive hyaluronan (HA) layer adsorbed onto the substrate. The absolute distance between the colloids and the surface was measured under flow with an accuracy of a few nanometers. We could verify the long-term prediction of classical lubrication theory for the movement of a sphere near a wall in a shear flow. The HA polymer layer exerted long-range repulsive steric force on the beads and the hydrodynamics at the boundary remained more or less unchanged. By incubating HA at various concentrations, the thickness of the layer, as estimated by beads most probable height, was tuned in the range 20–200 nm. Frequency of bond formation was decreased by more than one order of magnitude by increasing the thickness of the repulsive layer, while the lifetime of individual bonds was not affected. This study opens the way for further quantitative studies of the effect of molecular environment and separation distance on ligand-receptor association and dissociation.

INTRODUCTION

The glycocalyx is a polysaccharide-rich layer which decorates cell membranes and plays an important role in cell adhesion (1). It is composed of a large variety of glycoproteins, glycolipids, and sugar chains dangling from the membrane and it builds a complex polymeric structure exhibiting highly variable density and various degrees of branching and/or entanglement. Its thickness can vary from 10 to 20 nm in monocytes (2)—a length scale comparable to the length of most cell adhesion molecules, to a half a micron in endothelial cells (3) and up to few microns in chondrocytes (4). Measured thicknesses depend strongly on the preparation of the cells and the methods of observation, which include electron microscopy, dye exclusion, and microparticle image velocimetry (3,5).

Several studies support the view that the glycocalyx has an antiadhesive role. Removal of the glycocalyx by enzymes or genetic engineering facilitates cell adhesion (6), while increased expression of glycocalyx constituents impedes adhesion (7). The difference between the lengths of adhesion molecules versus repulsive molecules is a key parameter (7). A prominent example of the role of repulsive molecules in the control of specific cell response concerns the activation of T cell during the formation of the immunological synapse (8). Another important feature of glycocalyx is the difference between static and dynamic conditions. For example, the ability of P-selectin of various lengths on endothelial cells to bind to their ligand PSGL-1 on leukocytes varies according to whether conditions are static or dynamic: the repulsion exerted by the glycocalyx is more effective under flow (9,10). Another interesting aspect concerns the role of the effective viscosity of the layer on adhesion events. When two cellular surfaces approach, the solvent trapped between the surfaces has to be expelled to allow the close fitting of the membranes. The viscosity induced by the presence of sugar residues, which are either expelled or compacted during the cells approach, is likely to slow down the process by dissipative effects (5).

While some physical aspects of the role of the glycocalyx have been addressed with cells in vitro or in vivo (3), it is often difficult to distinguish unambiguously between these various effects in living systems. A physicochemical approach consists of building a model glycocalyx to assess the role of different physical parameters on adhesion: thickness of the polymer layer versus extension of the adhesive molecules, elasticity, and viscosity of the layer, area of the surfaces bearing the adhesion molecules, and shear rate in a presence of a flow. In this context, studies on polymer brushes have proved to be useful in research on antifouling or lubrication of artificial macroscopic surfaces, using the surface-force apparatus in shear mode (11). More realistic models of cell interfaces were realized with colloidal particles of cellular size (12). As an important component of the glycocalyx, the long chains of the disaccharide polymer hyaluronan (HA) have been used to create very soft polymer cushions (13). Thus, hyaluronan layers grafted to flat substrates have been described in terms of elasticity and viscosity using colloidal probes (14,15), with increasing degree of control of the substrate (12,16). A few experiments studied the combined effect of adhesive and steric repulsive forces on giant vesicles spreading (17,18). At the same time, interactions of ligands and receptors involved in cell adhesion have been explored in great detail at the single molecule level (19,20). Recent studies have shown a relation between

Submitted April 24, 2008, and accepted for publication May 29, 2008.

Address reprint requests to Laurent Limozin, E-mail: laurent.limozin@inserm.fr.

Editor: Thomas Schmidt.

0006-3495/08/10/3999/14 $2.00

doi: 10.1529/biophysj.108.135947

the conditions of bond formation and bond lifetime (21). Therefore, a detailed study of glycocalyx effects on single bond kinetics has become necessary. However, to our knowledge, reconstituted systems combining repulsive and adhesive units have not been yet studied at the single molecule level.

The method of choice to measure bond kinetics is the laminar flow chamber, where ligand-coated microspheres or cells are convected above a receptor coated-surface in a laminar flow at low shear-rate. Counting particle arrests yields information about molecular bond formation, whereas duration of arrest is related to bond lifetime. Forces in the pN domain are exerted on individual bonds, while parallel observation of many beads provides efficient statistics (22). To explore the mechanisms of bond formation between surface-attached molecules, a key quantity is the instantaneous distance separating the microbead from the surface (23). Hitherto in the flow chamber, this distance was calculated from the bead velocity using lubrication theory (23,24). However, a direct measurement is highly desirable, in particular in the presence of a glycocalyx, where lubrication theory used for the solvent cannot be a priori assumed to be valid. There are two surface optical microscopic techniques that provide nanometer sensitivity in sphere-surface distance measurement (henceforth referred to equivalently as bead height h), which can be combined with the large field of observation that is necessary for compatibility with flow chamber analysis. Total internal reflection microscopy (TIRM) (25) is based on the scattering by the bead of the fast decaying evanescent field away from the surface in total reflection illumination. Reflection interference contrast microscopy (RICM) (26) uses the Newton's rings produced by interference of rays reflected from the bead and from the surface. While these two techniques provide comparable precision in relative height determination, problems remain to be resolved to measure absolute distances. In the context of protein-ligand interaction, only a few reported works combine the use of RICM or TIRM/TIR fluorescence with colloidal force probe. For example, RICM was used with biomembrane force probe (BFP) (27) or atomic force microscopy (AFM) (28). More recently, movement of tethered Brownian spheres have been studied combining TIRM and flow chamber (29) or optical tweezers with TIR fluorescence microscopy (30) and RICM (31). However, to our knowledge, no studies of transient single molecule binding have been realized with simultaneous measurement of the reactive intersurface distance.

In this work, we have designed a reconstituted biomimetic system to measure the influence of long repulsive chains on the interaction of individual ligand-receptor pairs. We used laminar flow chamber assay to measure probability of formation and rupture of individual bonds between antibody-coated microspheres and antigen-coated surfaces decorated with hyaluronan. This was combined with the simultaneous measurement of absolute distance separating the two reactive surfaces by RICM. The article is organized as follows. We first present an original method of absolute distance calibration of RICM with AFM. This is validated on fixed or mobile beads by comparison with predictions of diffusion of a colloidal sphere near a wall in the absence of hyaluronan. The hyaluronan layer is then characterized in terms of repulsive potential, effective viscosity, as determined for two bead sizes and various shear rates. We show that the hyaluronan cushion thickness, as measured from average beads height, can be tuned by varying the concentration of incubating polymer, while the effective viscosity does not change noticeably. Finally measurements of adhesion frequency and detachment curves are presented for several cushion thicknesses.

MATERIALS AND METHODS

Materials

Beads

Two types of microspheres were used. IDC latex sulfate beads (Invitrogen, Cergy-Pontoise, France; diameter 9.6 μm, density 1.05, CV 7.4% as measured by flow cytometry) were passivated before use by an incubation of 30 min in bovine serum albumin (BSA; Sigma, St-Quentin Fallavier, France) at 3% (30 mg/mL). M450 Dynabeads (Invitrogen; diameter 4.5 μm, density 1.5, CV 2% by cytometry) were functionalized as follows: beads were rinsed once in borate buffer (0.1 M, pH 9), then incubated for 30 min in a solution of rat anti-mouse Fc fragment antibody (Serotec, Cergy-St-Christophe, France) at a concentration of 5 μg per 10^7 microbeads (in 0.1 M, pH 9 borate buffer) at 37°C under gentle stirring. BSA was then added at 1 μg/mL and incubation was continued overnight. After rinsing in phosphate buffer solution (PBS; Invitrogen), beads were incubated for 30 min in mouse anti-human ICAM-1 antibody clone (HA58; Ebioscience, San Diego, CA) or in the corresponding isotype control mouse antibody (Ebioscience, mouse $IgG_{1,\kappa}$). Before experiment, beads were rinsed once in PBS.

Substrates

All incubations, unless otherwise specified, were performed at room temperature. Cover slides of size 24 × 24 mm and corrected thickness 0.170 ± 0.01 mm (Hecht, Sondheim, Germany) were used. For experiments without Fc-ICAM-1 functionalization, the cover slides were cleaned by sonication in a solution of Hellmanex (Hellma, Paris, France) followed by multiple rinsings with ultrapure water and coated successively with poly-L-lysine (PLL; Sigma, 300 kDa) at 10 μg/mL in PBS during 30 min and hyaluronic acid (Sigma, 700 kDa) at 10 μg/mL in PBS to create a soft polymer cushion (18). For functionalization with Fc-ICAM-1 chimera, the cover slides were cleaned with a solution of 30% H_2O_2 (50% solution in water, Sigma) and 70% H_2SO_4 (Sigma) under stirring for 10 min, then thoroughly rinsed in ultrapure water. Cover slides were then incubated in PLL at 100 μg/mL in PBS during 30 min, rinsed in PBS, incubated in glutaraldehyde (2.5% v/v in PBS, Sigma) during 30 min, rinsed in PBS, and successively incubated in a 1 μg/mL mouse anti human Fc antibody in PBS for 30 min, and in a blocking solution of 0.2 M glycine (Sigma) in 0.1 M phosphate buffer, pH 7.2 for 1 h. They were rinsed, then incubated in human Fc-ICAM-1 chimera (R & D Systems Europe, Lille, France) solution for 30 min at different concentrations varying between 0.005 and 0.2 μg/mL. Cover slides were then rinsed in PBS and passivated in 10 μg/mL BSA solution in PBS, or incubated in hyaluronic acid solution in PBS then rinsed in PBS and finally passivated in 10 μg/mL BSA solution in PBS. In some experiments, hyaluronan layers were treated with the enzyme hyaluronate lyase (Sigma). The final molecular coating of substrates and beads is schematized on Fig. 1 *B*. The density of

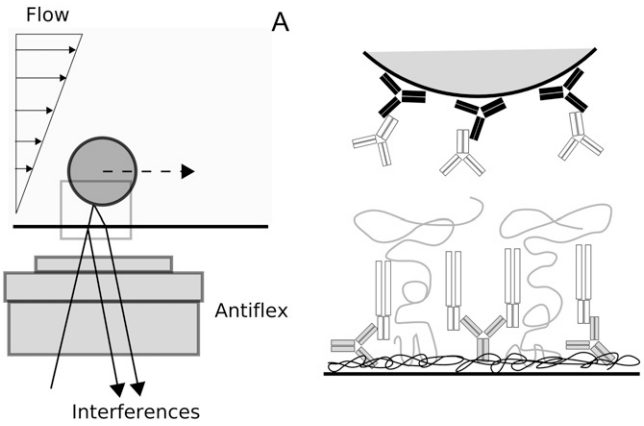

FIGURE 1 Principle of coupled laminar flow chamber and reflection interference contrast microscopy (RICM) in presence of adhesion molecules and an artificial glycocalyx. (*A*) RICM is performed on micrometer-sized beads in shear flow. (*B*) Beads are coated with a double-layer of antibodies recognizing Fc-ICAM-1 attached to the substrate through a first layer of antibody. Adsorbed hyaluronan mimics the glycocalyx.

Fc-ICAM-1 molecules grafted to the surface was estimated by measuring the fluorescence after direct labeling with a fluorescent antibody (Ebioscience, HA58-phycoerythrin). The amount of fluorescence was calibrated by measuring bulk solution containing diluted antibody between coverslip and cover slide. The surface density after incubation of Fc-ICAM-1 at the typical concentration of 0.01 μg/mL during 30 min was estimated at $\sim$2 molecules/μm^2.

Flow chamber

The flow chamber consisted of a hollow copper bottom onto which the cover slide is pressed by a Plexiglas top with an O-ring for sealing and enclosing a compartment of dimensions $15 \times 6 \times 0.17$ mm. The flow of PBS + 0.2 μg/mL BSA induced by a syringe varied between 1 and 28 s^{-1}. The bottom of the chamber allows access to oil immersion objective for RICM observation. The chamber was put on a homebuilt three-screws stage to ensure a correct orthogonality of the sample with the optical axis.

Optical microscopy and data acquisition

An inverted microscope in bright-field illumination equipped with a 20$\times$ lens and a standard video camera was used to follow the two-dimensional trajectory of the beads and to measure their adhesion to the underlying substrate. Video signal was digitalized at video rate (25 Hz) by a digitalization card (Hauppauge, Paris, France) and compressed on-the-fly by the DivX codec and the freeware VirtualDubMod. Beads trajectories were tracked off-line by a homemade program written in C++ and operating on disinterlaced compressed DivX sequences. Two-dimensional bead trajectories were retrieved with a 20 ms timestep and $\sim$40-nm lateral resolution. Statistics of molecular bond formation and rupture were determined by counting the frequency and duration of beads arrest events in the laminar flow as previously described (22). Briefly, a bead was considered to be arrested if its position did not change by more than $\delta x = 0.5$ μm in $\tau = 0.2$ s, and if its velocity before the arrest corresponded to that of a moving sedimented bead.

The adhesion frequency was defined as the number of arrests divided by the total time spent by the beads after sedimentation in the velocity range defined before. An arrest was considered to continue as long as the arrest criterion was satisfied, which yields an apparent duration d_{app}. The true arrest duration d_{true} was obtained with the correction $d_{\mathrm{true}} = d_{\mathrm{app}} + \tau - 2\delta x/v$, where v is the most probable velocity of the beads (22). The detachment curve was built by counting the fraction of arrests exceeding the duration t.

For the static adhesion assay, the flow chamber was prepared as for dynamic adhesion assay. The bead suspension was injected into the chamber, and was allowed to sediment without any flow. The beads were displaced by imposing a brief high shear stress, and were allowed to rest again for 10 s. At the end of the resting time, a shear stress of 28 s^{-1} was set to detach the beads. Adherent beads were detected by comparing their position during the resting period and after restarting the flow. The proportion of bead attached was calculated, accounting for the beads not displaced by the initial high shear stress.

Time-lapse RICM was performed on an inverted microscope (Axiovert 200; Zeiss, Jena, Germany) for RICM with a XCite 120 light source (Exfo, Mississauga, Ontario, Canada) in epi-illumination, a bandpass green filter 546 $\pm$ 12 nm (Chroma, Rockingham, VT), an Antiflex 63$\times$ objective and a polarizing cube (Zeiss). The illumination aperture diaphragm was set at the minimal opening for measurements (corresponding to an illumination numerical aperture equal to 0.32). The camera used for the AFM calibration was either a Sensicam (PCO, Kelheim, Germany) run with the software Openbox (32) or a C7780 run with the software Wasabi (both Hamamatsu, Massy, France). Recordings in flow (Fig. 1 *A*) were realized using an iXon camera (Andor, Belfast, UK) run with a custom-built software under Labview (National Instruments, Nanterre, France). The typical frame rate used was $fps = 45$ Hz, and the typical exposure time was $t_{\mathrm{exp}} = 20$ ms. The focus was reached automatically by maximizing the contrast of the field diaphragm. The horizontality of the sample was realized by successive adjustments of the three screws of the chamber holder. The final deviation of the focus on all parts of the sample was $<$50 nm. As shown on Fig. 2, RICM of a micrometer-size sphere hovering above a surface give rise to circular interference fringes (Newton's rings) of micron size, whose radius depends on sphere-surface distance and the radius of the sphere (for given wavelength and illumination numerical aperture). Typical interference patterns for the two types of beads used are shown in Fig. 2, *A* and *C*.

RICM data analysis and height calibration

Tracking of bead center and RICM fringes

The position of the center of a bead observed in RICM was determined using an algorithm which seeks the center of symmetry of the fringe pattern (32) (implemented in Igor Pro 5, WaveMetrics, Portland, Oregon). Briefly, the sum of the standard deviations of the intensity along successive concentric circles was calculated. The calculation was repeated by taking the center of the circles on every pixels around an initial guess. The matrix of the sums calculated from each pixel-center was built. The center of symmetry was determined with subpixel accuracy as the location of the minimum of the three-dimensional paraboloid interpolating the matrix around its minimum value. For the tracking of a timelapse sequence, the center found in the previous image was used as guess for the next image. In case of the AFM calibration, the initial guess of the center was chosen by the user on the first image. Depending on the relative position of the bead with respect to the cantilever, part of the fringes could be hidden by the strong reflection of light on the cantilever. In this case, the symmetry was not calculated by summing on all angles, but only for a angular sector defined by the user, limiting the research of extrema to the visible part of the fringes. In case of the flow chamber assay, new beads reaching the field of view were automatically

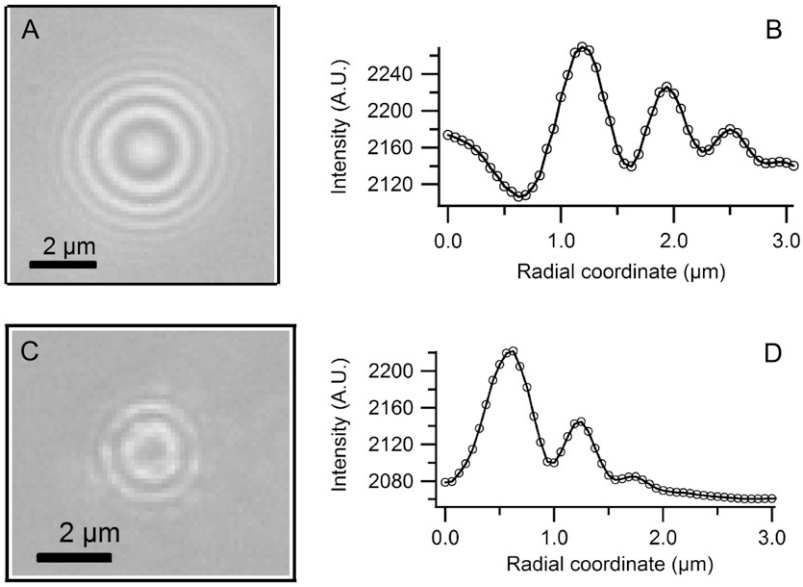

FIGURE 2 RICM fringes obtained with two types of microbeads. (*A* and *C*) Raw RIC micrographs of interference fringes from microspheres taken in typical conditions: latex IDC 9.6 μm diameter (*A*), and M450 4.5 μm diameter (*C*). (*B* and *D*) Corresponding intensity radial profile taken from the center of symmetry of the rings, averaged on angles. Bead-substrate distance is retrieved from the position of the fringes extrema.

detected at regular time intervals and their center of mass was approximately found by standard image treatments. This position was used as guess for further subpixel determination which was then performed on the raw image sequence as described above. The algorithm used to find the center of symmetry simultaneously calculated the average radial profile of intensity. The precise positions of the extrema of intensity corresponding to each fringe were determined by locally fitting the profile with a parabola. For 9.6 μm beads, the position of the first three maxima and three minima were stored (only two maxima and two minima were stored for 4.5 μm beads). Typical interference profiles obtained for the two types of beads used are shown in Fig. 2, *B* and *D*.

Bead-substrate distance calibration

The calibration was used to determine the relation between the radius of RICM fringes and the absolute bead-surface separation. To measure this relation directly, a bead was moved vertically relatively to the surface, and the fringe pattern obtained in RICM was simultaneously recorded (Fig. 3 *A*). For this purpose we used an atomic force microscope Nanowizard I (JPK, Berlin, Germany) in closed-loop force mode. A bead was stuck to the end-side of a cantilever (MLCT; Veeco, Plainview, NY; nominal spring constant 10 mN/m) using micromanipulation (33). After the bead-substrate contact was established (corresponding to a maximal applied force of ~10 nN), a series of force curves were recorded, each force curve representing 4096 values of the cantilever deflection as a function of the piezoelectric vertical position during approach and retraction for a traveling range of typically 500 nm, at a velocity of 100 nm/s. A typical raw force curve is showed in Fig. 3 *B*. The part of the curve corresponding to the contact bead-cantilever (where the deflection in V is proportional to the piezo displacement) was fitted by a straight line which slope gives the relation between deflection measured in V and deflection in meters (also called sensitivity). The deflection in meters was added to the piezo distance to provide the bead-surface distance (BSD). The raw force curve was rectified to express the deflection in meters as a function of the BSD (*rectified force curve*, Fig. 3 *C*). For the entire RICM sequence recorded, the radius of the first six extrema of the intensity fringes were tracked as described in the previous section. The BSD and the extrema positions as a function of time were synchronized at the position where the piezo starts the approach, yielding a time uncertainty of <1 frame duration, corresponding to a maximal height error of 2.5 nm. The BSD h was further plotted as a function of each of the extrema radii r_i (Fig. 3 *D*). Each curve was fitted with the function

$$h(r_i) = \frac{l_i\lambda}{4n} - R_{\mathrm{eff,i}} + \sqrt{R_{\mathrm{eff,i}}^2 - r_i^2}, \qquad (1)$$

which corresponds to the dependence $h(r)$ given by the simple RICM theory (32), with λ the light wavelength and n the medium refractive index. This yielded for each extremum two fitting coefficients: an effective bead radius $R_{\mathrm{eff,i}}$ and a fringe order l_i. These coefficients were measured from force curves repeated up to six times in different locations of the sample and for five different IDC beads. The radii of the beads measured from bright-field illumination micrographs varied from 4 to 5.4 μm. The same procedure was applied to calibrate the M450 beads, using three measured beads of identical radius. The values of the calibration coefficients $R_{\mathrm{eff,i}}$ and l_i obtained for the different beads are summarized in Fig. 3 *E*. These values were linearly interpolated as a function of the bead radius R to provide functions $R_{\mathrm{eff,i}}$ and a fringe order l_i for each extremum i. For example, coefficients for the second extremum of IDC beads are given by $R_{\mathrm{eff},2} = 1.409 + 0.073R$ and $l_2 = -3.795 \times 10^{-7} + 1.093 \times 10^{-6}R$; and for M450 beads by $R_{\mathrm{eff},2} = 1.59$ and $l_2 = 2.68 \times 10^{-6}$.

Bead height determination using the calibration

The time-dependent height of a bead was determined after tracking the bead center and the fringe positions for the entire recorded sequence. The fringe order was defined by numbering the fringes of a calibration bead in contact with the substrate, starting with the first maximum, etc. For a bead fluctuating in height, the order was determined by searching the lowest extremum reached. The bead height was then calculated using the first successive nondisappearing extrema and coefficients of the calibration table. The actual bead radius was selected to minimize the difference between heights calculated from two successive extrema. With this method, one could retrieve the height of a fluctuating bead between 0 and 300 nm. To check visually that the choice of order was correct, the curves of the intensity at the center with the reconstructed height were plotted and compared with a similar curve $I(h)$ computed for the calibration beads. It should be noted that for symmetry reasons, $I(h)$ is independent of the bead radius.

Diffusional analysis of three-dimensional trajectories

The diffusional properties of beads were obtained from analysis of experimental three-dimensional trajectories as follows. Heights h were binned in

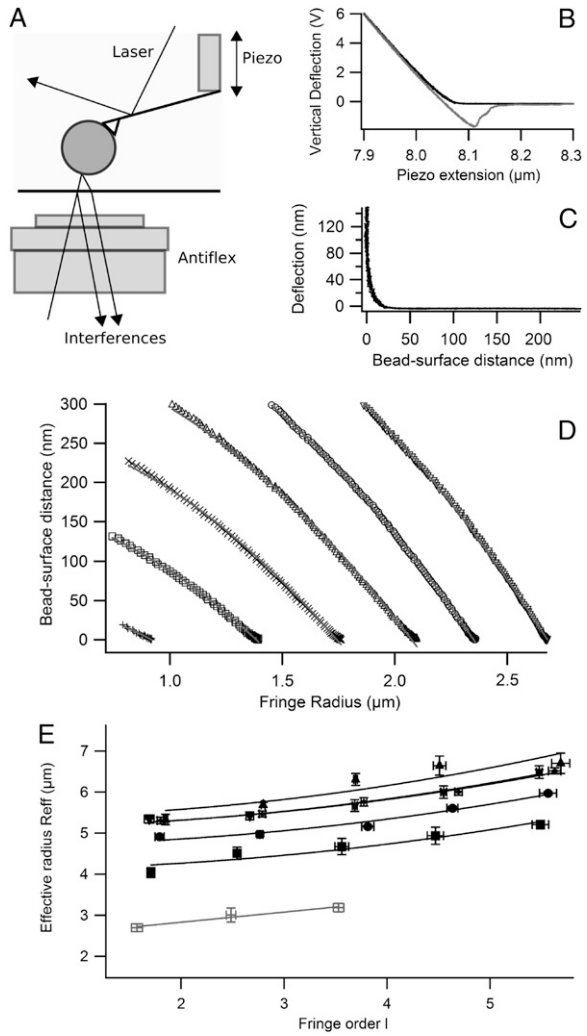

FIGURE 3 Principle of bead-substrate distance calibration with atomic force microscopy (AFM). (*A*) A bead attached to the tip of a cantilever is moved vertically while recording simultaneously cantilever deflection and fringes in RICM. (*B*) Typical force curve showing the cantilever deflection during push (*solid*) and retract (*shaded*) movement of the substrate toward the bead. (*C*) Rectified force curve after calibration of deflection and determination of zero bead-substrate distance. (*D*) Bead substrate distance obtained from panel *C* plotted as a function of fringes radii measured from RICM sequence. Curves are fitted according to Eq. 1 yielding for each extremum and each bead radius an effective bead radius $R_{\mathrm{eff,i}}$ and a fringe order l_{i}. (*E*) Plot of $R_{\mathrm{eff,\,i}}$ versus l_{i} obtained with eight different beads: five IDC of various diameter (*solid symbols*) and three M450 of identical diameter (*shaded symbols*). Error bars are SD obtained from repeated force curves measured on beads of identical diameter.

stacks of equal thickness δh (typically $\delta h = 10$ nm). The distribution of displacements Δ_α (in one of the directions $\alpha = x, y,$ or z; x parallel to the flow and z vertical) during the time interval τ at a starting height h was computed and fitted with a Gaussian function, following (34,35)

$$P(h,\Delta_\alpha,\tau|h,0) = [4\pi D_\alpha \tau]^{-1/2}\exp\left(-\frac{[\Delta_\alpha - v_\alpha(h)\tau]^2}{4D_\alpha(h)\tau}\right), \quad (2)$$

which is valid for short times τ, where D_α is a diffusion coefficient and v_α a drift velocity. The value τ was varied between the duration of one frame (20 ms) and three frames (60 ms) and D_α, v_α were retrieved from linear fit of the coefficients $v_\alpha(h)\tau$ and $4D_\alpha(h)\tau$ with τ, taking into account the uncertainty on these coefficients obtained from the Gaussian fit.

RESULTS

Beads height distributions and diffusion without flow

The resolution of the three-dimensional trajectory reconstruction was first tested on beads attached to the substrate. On cover slides coated with BSA or PLL, uncoated clean IDC beads adhered immediately after sedimentation and did not exhibit any visible motion. Height data were then accumulated for several beads during tens of seconds. The distribution of beads heights was approximately Gaussian with $h = 0 \pm 6$ nm ($\pm$SD) on BSA and $h = -12 \pm 5$ nm on PLL. The standard deviation of height in such a population of beads is mainly due to interbead variability. For a single bead trajectory, the standard deviations are $\delta x = \delta y \leq 2$ nm and $\delta z \leq 3$ nm, which sets the resolution of position determination of an immobile bead. In these conditions, the diameters of IDC beads retrieved from the fringes correlate satisfactorily with those directly measured in bright-field, with a maximal discrepancy of 0.3 μm.

The height distribution of BSA-coated IDC beads was measured after sedimentation on substrates coated with PLL + antibody + BSA. In this case, beads exhibited long timescale Brownian motion and only rarely adhesion events. Trajectories showing adhesion were removed from the statistics. A typical field of view exploited in the present measurements is shown on Fig. 4 *A*. The cumulated height positions of ~20 beads observed during 20 s are shown on Fig. 4 *B*. Solid line on Fig. 4 *B* is an exponential fit of the equilibrium distribution of the form $p(h) \sim \exp(h/h_{\mathrm{b}})$, with $h_{\mathrm{b}} = mg/k_{\mathrm{B}}T$, with g the acceleration of gravity, and $k_{\mathrm{B}}T$ the Boltzmann factor. It yields the average bead mass $m = (4\pi/3)R^3\Delta\rho$, with the relative density $\Delta\rho = 0.05$ and an average bead radius $R = 4.9$ μm (close to the nominal radius of 4.8 μm). The height distribution of BSA-coated IDC beads on PLL + HA is also shown on Fig. 4 *B* and is consistent with previous measurements on similar substrates (18).

Diffusion coefficients of IDC beads were measured using the analysis associated with Eq. 2 and based on data obtained from several trajectories, for a total of 20,000–50,000 positions. Fig. 4 *C* shows the values of horizontal diffusion coefficients D_{x} (x direction from *right* to *left* in Fig. 4 *A*) and D_{y} (y direction from *bottom* to *top* in Fig. 4 *A*). The discrepancy between D_{x} and D_{y} at a given height is an indication of the error in measurement and is highly dependent on the statistical weight at this height (refer to the *bars* for the height distribution on Fig. 4 *C*). The underlying substrate was coated either with PLL + antibody + BSA (*solid symbols* corresponding to smaller heights) or PLL + HA (*open symbols* corresponding to larger heights). The variation of the vertical

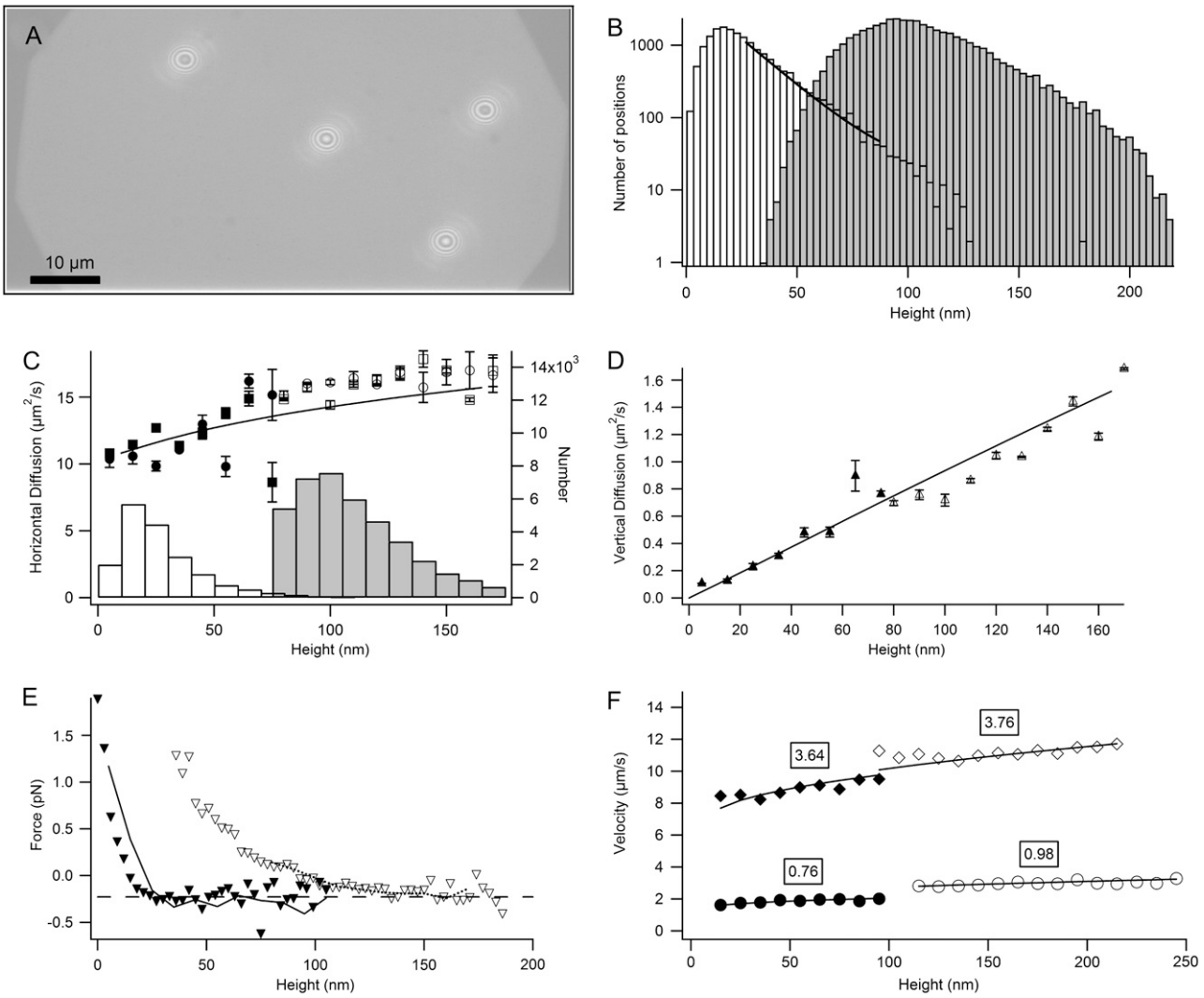

FIGURE 4 Diffusion and interaction with the surface for BSA-coated 9.6-μm latex beads in absence or presence of a repulsive HA layer. (*A*) Typical field of view in RICM and flow conditions showing the field diaphragm and the fringes of four IDC beads. (*B*) Beads height distribution on substrates coated with PLL + antibody (*open bars*) or PLL + HA (*shaded bars*). (*C*) Horizontal diffusion coefficients D_x and D_y as a function of height: without HA (D_x, *solid circles*; D_y, *solid squares*), with HA (D_x, *open circles*; D_y, *open squares*). Height distributions identical to panel *B* are also shown. The line is the prediction of lubrication theory, in absence of polymers. (*D*) Vertical diffusion coefficient D_z as a function of height: without HA (*solid triangles*) or with HA (*open triangles*). The line is the prediction of lubrication theory, in absence of polymer. (*E*) Force-exerted beads as a function of height without HA (*solid triangles*) or with HA (*open triangles*), and deduced from equilibrium distribution (see panel *B*). The line is the force calculated from the vertical diffusion coefficient and vertical drift velocity and using Einstein's relation. The dashed line represents the gravity force only. (*F*) Velocities along the flow as a function of height without HA (*solid symbols*) or with HA (*open symbols*). The line is the prediction of lubrication theory, in absence of polymers and for values of the shear rate indicated in the boxes.

diffusion coefficient D_z with height, measured in similar conditions, is shown on Fig. 4 *D*.

The prediction of the classical lubrication theory describing the diffusion of a sphere near a wall was compared to the measurements. The following approximated formulas were used: $D_x(h) = D_0/F_x(h, R)$ and $D_z(h) = D_0/F_z(h, R)$. It was assumed that all the beads have identical nominal diameter R and that all surfaces are perfectly smooth, without polymer coating, so that the viscosity is $\nu = \nu_{water}$. $D_0 = (k_BT/6\pi R\nu)$ is the bead diffusion coefficient far from the surface. The coefficients

$$F_x(h,R) = \exp[0.00332\ln^3(h/R) + 0.0193\ln^2(h/R) - 0.183\ln(h/R) + 0.327]$$

and

$$F_z(h,R) = \exp[0.00577\ln^3(h/R) + 0.0922\ln^2(h/R) - 0.527\ln(h/R) + 0.770]$$

were obtained from fits of numerical results (24). The theoretical diffusion coefficients compare well with the experiments (*solid lines* in Fig. 4, *C* and *D*), with or without

hyaluronan coating. This proves the accuracy of the absolute height determination of diffusing IDC beads with a typical error of <5 nm. In this respect, it is also instructive to estimate the effect of finite exposure time $t_{exp} = 20$ ms on measurements. The displacements due to bead diffusion at ~100-nm height during t_{exp}, are, respectively, 17-nm horizontally and 5-nm vertically, which sets the resolution of the method for diffusing beads.

Vertical force exerted on the beads

The interaction potential $V(h)$ between beads and surface was retrieved from the equilibrium distribution through $p(h) \sim \exp(-V(h)/k_BT)$. In Fig. 4 *E*, the vertical force calculated as $F(h) = -dV/dh$ is plotted as a function of height for the two substrates coatings (*symbols*). The force is repulsive at short distances and reaches asymptotically the pure gravity at large heights (*dashed line* in Fig. 4 *E*). Alternatively, the vertical force was calculated from Einstein's formula $F = k_BTv_z(h)/D_z(h)$, where D_z is the vertical diffusion coefficient and v_z is the drift velocity in the vertical direction, both measured using Eq. 2. The force calculated with this method is plotted as a solid line in Fig. 4 *E* and shows a good agreement with the values deduced from the interaction potential. This confirms the reliability of the force measurement obtained with two different methods, and the validity of the diffusion measurements.

Horizontal velocity of the beads in flow

While previous measurements were realized in the absence of flow, horizontal velocity in the direction of the flow v_x was also measured when various shear rates were applied in the chamber. The dependence of v_x with height was computed using Eq. 2 in the absence or presence of HA. Results are presented on Fig. 4 *F*. Experimental data was fitted using the lubrication theory with the shear rate G as only adjustable parameter (*solid lines* in Fig. 4 *F*). The theoretical dependence reads as $v(h) = R \times G \times F_v(h)$, where R is the bead radius and

$$F_v(h) = \exp[0.00376\ln^3(h/R) + 0.0723\ln^2(h/R) + 0.548\ln(h/R) + 0.689]. \quad (3)$$

Values of G are consistent with values deduced from the flow imposed by the syringe and chamber size, when the shear rate G in the range 0–7 s^{-1}. The slight discrepancy occurring for the lower heights could be explained by the polydispersity in bead sizes, since larger beads may be lower but experience a higher flow at their center of mass.

Tuning of hyaluronan layer thickness and apparent viscosity

The incubating concentration of hyaluronan was systematically varied in the range 0–1 μg/mL. BSA-coated IDC beads or M450 beads coated with the isotype control antibody were allowed to sediment on the top of the polymer layer. Additionally, shear was applied with shear rate values ranging from 0 to 5 s^{-1}. In each case, the height distribution was measured with RICM and found to exhibit similar shape as in Fig. 4 *B*. The most probable height h^* was determined as the location of the maximum of the histogram with a precision of ± 5 nm for IDC beads and ± 10 nm for M450. The error is higher for M450 beads due to the poorer quality of the calibration. The value h^* increases regularly with incubating HA concentration (Fig. 5 *A*). Values range from ~20–40 nm in the absence of HA to almost 200 nm in the presence of a polymer layer formed at 1 μg/mL incubating HA. The value

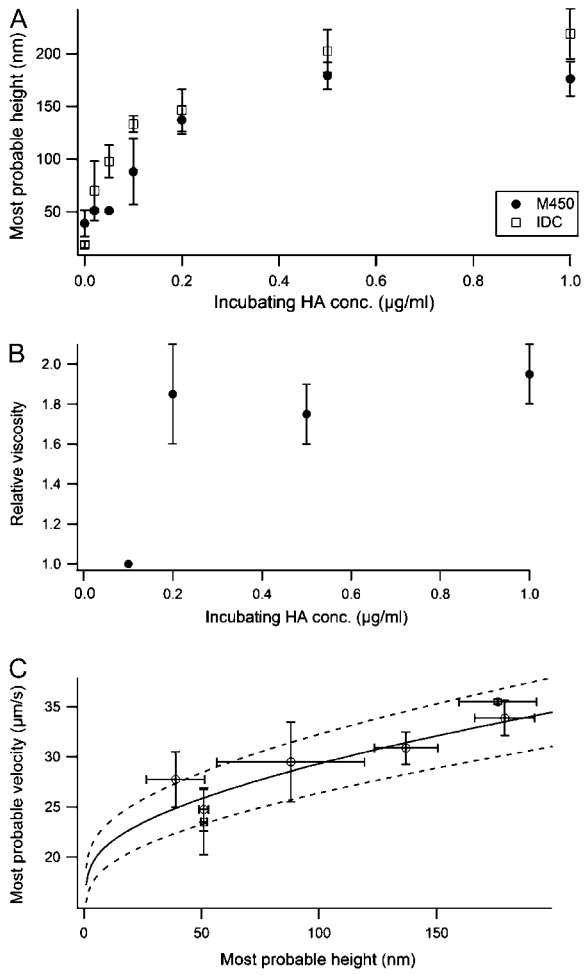

FIGURE 5 Tuning of hyaluronan layer properties by varying the concentration of incubation. (*A*) The most probable height of 9.6 μm (*open square*) or 4.5 μm (*solid disks*) beads as a function of the incubating concentration of HA. Error bars are standard deviations of measurements obtained on various samples with various shear rates. (*B*) Relative viscosity extracted from the slope of $D_z(h)$ as a function of the incubating concentration of HA. (*C*) Most probable velocity of M450 beads as a function of their most probable height, when the incubating concentration of HA is varied. The solid line is the prediction of the lubrication theory in the absence of polymers and for a shear rate of 20 s^{-1}. Dashed lines are theoretical curves obtained for shear rates of 18 or 22 s^{-1}.

h^* shows a slight but systematic increase for increasing values of the shear rate, of the order of 10–30%. The values h^* of M450 are systematically lower than h^* for IDC.

The apparent viscosity ν was estimated for various HA layers in the absence of flow. For this, the vertical diffusion coefficient D_z was measured as a function of height as described above. Looking at the quasilinear relation on Fig. 4 *D*, a reasonable approximation is $D_z(h) = (k_B Th/6\pi\nu R^2)$, where ν is the apparent viscosity supposing an homogeneous medium under the bead and R is the nominal bead radius. As shown before, the relative viscosity measured with IDC beads does not differ from that of water even in the presence of polymers: $\nu/\nu_{water} \sim 1$. However, the relative viscosity, when measured with M450 beads, exhibits values significantly greater than 1 when [HA] ≥ 0.2 μg/mL, as shown in Fig. 5 *B*.

In the presence of an applied flow and for various HA layer thicknesses, the distributions of velocities in the direction of the flow were measured. They exhibited a maximum for nonvanishing velocity, as previously observed (36). This most probable velocity v^* is plotted as a function of the most probable height h^* for various incubating concentrations of HA (Fig. 5 *C*). The results were compared with the prediction of the lubrication theory relating the velocity and the bead height. Solid line in Fig. 5 *C* is obtained from the theory using a shear rate of $G = 20\ s^{-1}$. To estimate the uncertainty, theoretical curves for $G = 18\ s^{-1}$ and $G = 22\ s^{-1}$ are represented with dashed lines. All theoretical values of G are noticeably smaller than that predicted from the chamber size and shear rate at $28\ s^{-1}$.

The role of the HA molecules in repulsion was directly tested by digesting the polymer chains with the specific enzyme hyaluronase (HAase). After 10 min of incubation of HAase at an activity of 10 U on a thick HA layer (obtained as described before, with 1 μg/mL HA incubated for 30 min), beads initially at ~200 nm height fall to ~20 nm. The height distribution after of HAase treatment is similar to that obtained in absence of incubated HA.

Single bond formation through the hyaluronan layer

The adhesion of functionalized M450 beads to the underlying substrate coated with Fc-ICAM-1 was studied for various HA coverages. Positive adhesion assay was performed using M450 coated with anti-ICAM-1. Negative assay was performed on the same substrate with beads coated with a control isotype. Specific adhesion frequency was defined as positive minus negative frequencies (36). First the conditions for single bond formation and rupture were determined as follows. Successive dilutions of Fc-ICAM-1 on the substrate lead to a regime, at an incubation concentration [Fc-ICAM-1] ≤ 0.01 μg/mL, where specific adhesion frequency varied proportionally with the Fc-ICAM-1 density. In this regime, the detachment curves showed no variation with further Fc-ICAM-1 dilution, indicating that the nature of the bond-rupture remained identical.

Positive and negative adhesion frequencies were measured for various HA coatings and a shear rate of $G = 28\ s^{-1}$. Both were found to decrease by almost two orders of magnitude when the incubating HA concentration was raised from 0 to 1 μg/mL (Fig. 6 *A*). The number of arrest events considered ranged from a few hundreds at low HA concentration to a few tens at high HA concentration. The ratio of positive/negative adhesion frequencies varied typically between two and four. Error bars δFA_{pos} and δFA_{neg} are standard deviations of values obtained on at least three different samples for each condition.

Detachment curves for different HA coverages are shown in Fig. 6 *B*. Each curve was built with several hundreds of rupture events. The rupture process appears to be roughly biphasic, with a change of rate of detachment at ~1 s. The variations in bound fraction in the first five seconds of binding differed by <10% between the various conditions: [HA] = 0, 0.02, and 0.1 μg/mL, indicating that the nature of the bond rupture was not noticeably affected by the presence of the HA layer.

The specific adhesion frequency of functionalized M450 at [Fc-ICAM-1] ≤ 0.01 μg/mL and $G = 28\ s^{-1}$ is plotted as a function of the beads most probable height for various HA coverages (Fig. 6 *C*). Most probable heights have been measured as described previously. Error bars on specific adhesion frequencies are calculated as $\delta FA_{spe} = \sqrt{\delta FA_{pos}^2 + \delta FA_{neg}^2}$.

Adhesion was also measured in static conditions by counting the proportion of beads, initially at rest for 10 s, which were nondetached by a flow of $G = 28\ s^{-1}$. Both positive and negative adhesion were found to decrease by one order of magnitude when the incubating HA concentration was raised from 0 to 1 μg/mL (Fig. 6 *D*). Each data point was calculated by counting ~500 beads.

Simultaneous measurement of instantaneous height and velocity

The classical criterion used in flow chamber to define a binding event is that the velocity is less than a given threshold, fixed here at $v_s = 2.2$ μm/s. To compare the events detected with this method with the proximity between the two reacting surfaces, an alternative criterion based on height was defined. Thus, events of close-contact occurred when a bead approached the surface at a height $h \leq h_s$ and remained at $h \leq h_s + \delta h_s$. The value δh_s accounts for height fluctuations of a bound bead. To correct for bead-to-bead variations in absolute height, the zero height reference for a given bead was taken as the average height during the arrests defined by the velocity criterion.

In Fig. 7, *A* and *B*, are shown the representative trajectories for height and velocity of two M450 beads, functionalized with anti-ICAM-1, hovering above the substrate coated at [Fc-ICAM-1] = 0.01 μg/mL and [HA] = 0.05 μg/mL. The shear rate was fixed at $G = 7\ s^{-1}$. In Fig. 7 *A*, the velocity exhibit two periods where $v \leq 2.2$ μm/s (*dashed line*), cor-

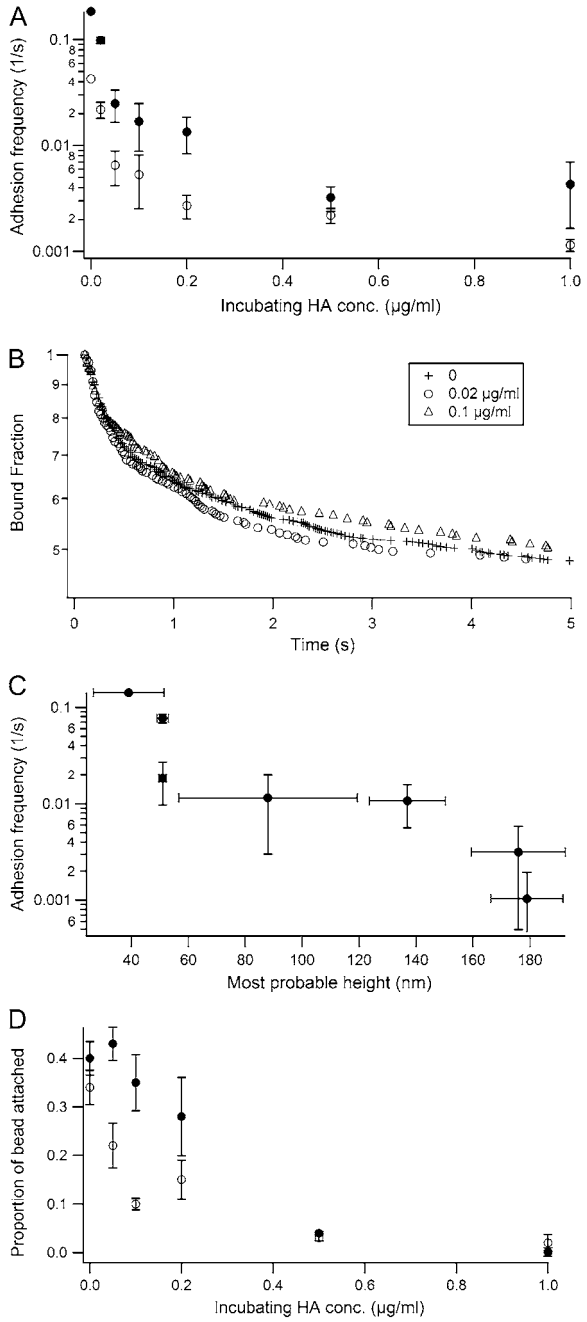

FIGURE 6 Adhesion through hyaluronan layers of variable thickness. (*A*) Frequency of adhesion (number of arrests per second) of 4.5 μm beads functionalized with Anti-ICAM-1 (*solid circle*, positive) or an isotype control antibody (*open circle*, negative) to a surface coated with Fc-ICAM-1 and hyaluronan layer formed at variable concentration of incubation. Shear rate $G = 28\ s^{-1}$. Error bars are standard deviations of values measured on at least three samples in identical conditions. (*B*) Detachment curve showing the fraction of arrested beads functionalized with Fc-ICAM-1 that are still arrested after the time in abscissa. Incubating concentrations of HA are 0 (*crosses*), 0.02 (*circles*), and 0.1 μg/mL (*triangles*). (*C*) Specific adhesion frequency of M450 beads (defined as positive minus negative adhesion frequency) as a function of the most probable height, for variable hyaluronan coatings. (*D*) Proportion of 4.5 μm beads, initially immobile during 10 s, which are nondetached by a flow of 28 s^{-1} (same symbols as in *A*). Error bars are mean $\pm$ SE.

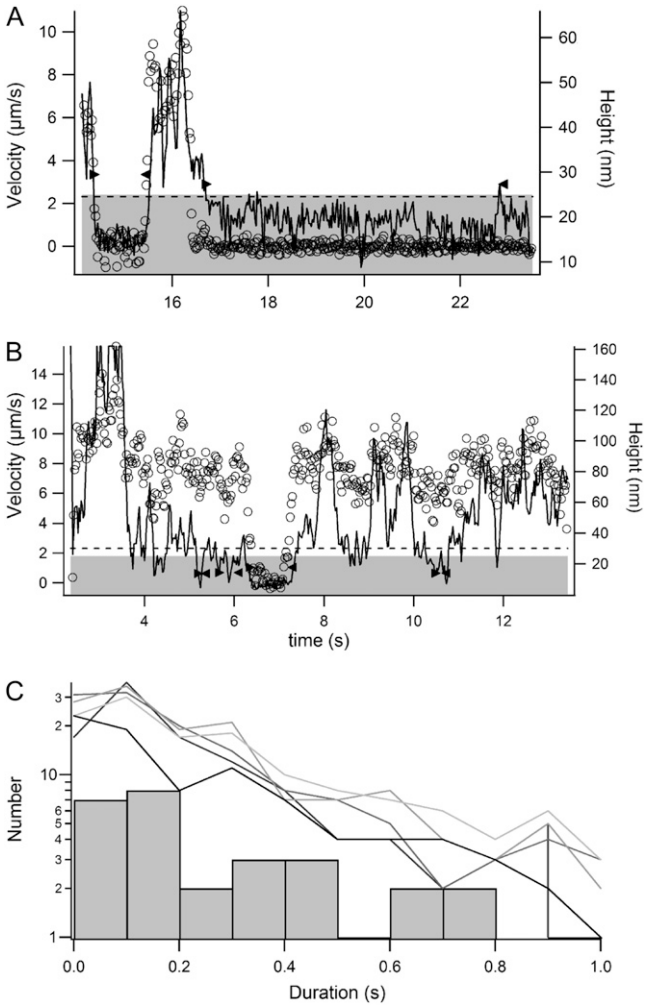

FIGURE 7 Simultaneous measurement of velocity and height trajectories and criterion for binding. (*A* and *B*) Two typical trajectories of an anti-ICAM-1 coated 4.5-μm bead hovering above a ICAM-coated surface and a hyaluronan layer, and showing binding events. The velocity as function of time (*circles*, *left axis*) was calculated on four successive frames. The dashed line shows the velocity cutoff used to determine arrest events. The time-dependent height is represented on the right axis (*solid line*). The shaded zone indicates the heights below which the bead is considered in close contact. The arrowheads represent the start and end of events determined with the height criterion. (*C*) Histograms of the durations of events as determined with the velocity criterion (*shaded bars*) or with the height criterion (*solid lines*) for height threshold values 5, 10, 15, 20, and 25 nm (from *solid* to *light shaded*).

responding to two arrests. The criterion of binding with height, with $h_s = 10$ nm and $\delta h_s = 15$ nm, identified two close-contact events which are superimposed to the velocity arrests. In Fig. 7 *B*, one arrest was detected with the velocity, while four close-contacts were detected with the height. This illustrates the additional information gained by the measurement of height, as discussed later.

The two criteria were used to define the distribution of arrest and close-contact durations in a population of 100 beads in the conditions defined above for the beads of Fig. 7, *A* and *B*. The close-contact events defined using the height

are roughly two times more numerous than the classically counted arrest events and their durations distribute roughly in a exponential manner (Fig. 7 *C*). To assess for the role of the arbitrary threshold h_s used to define the height threshold, it was varied between 5 and 25 nm. Only the distribution of close-contact events found with $h \leq h_s = 5$ nm show a significant reduction of the number of events detected, while all distributions for the other thresholds were similar, indicating no strong influence of $h \leq h_s$ beyond 10 nm.

DISCUSSION

Validation of the RICM-flow chamber and alternatives

We discuss here the challenges which led us to choose the proposed techniques. Firstly, the study of single-bond formation and rupture should rely on the statistics of a large number of events, which is tedious to retrieve with single-probe techniques like biomembrane force probe (BFP) (19), AFM, or optical tweezers. The flow chamber offers a faster approach based on the parallel observation of multiple events on a wide microscopic field. In the problem of bond formation, the distance separating the reactive surfaces is of crucial importance (23,37). The measurement of this distance has a poor resolution with BFP (38) and is only indirect with AFM, based on the location of the hard-wall repulsion of the surface. For optical tweezers, it is often based on back focal-plane interferometry, which gives only the distance of the bead relative to the focal plane and not to the surface (39). Colloidal probes are the most sensitive force sensors, which rely on equilibrium height distributions to evaluate the interaction potential (25). Recent reports confirm the excellent resolution of the technique (40,41) to measure forces in the range of a few tens of fN. To measure the bead-substrate distance, the main tool is total internal reflection microscopy, based on the scattering of the evanescent wave by the colloid (TIRM (25)). This technique reliably measures the relative distance from the scattered intensity. The usual method to determine absolute height is either to induce colloid binding at the end of the observation (42) or to rely on the dependence of the vertical diffusion coefficient with height, based on lubrication theory (25,34). Moreover, in the latter case, the bead radius should be measured independently. None of these methods are appropriate in the present situation, since transient interactions in an environment of unknown hydrodynamic properties are to be probed.

Alternatively, the bead-substrate distance can be measured with RICM (14,15,43,44). While the technique is not new, the challenge of measuring absolute distances efficiently remains. The conventional method relies on calculating the interference pattern from the laws of refraction (26,44). However, some discrepancies between experimental and theoretical radial intensity profiles have been identified, especially for distances shorter than 20 nm or small bead diameters (26,31).

For these reasons, we set out to measure the bead-substrate distance directly by calibrating it in the range 0–200 nm, using the controlled movement of a bead stuck to an AFM cantilever. The calibration was performed for two types of beads in absence of antibody and polymer coating. Our main assumption that the calibration is also valid in the presence of the artificial glycocalyx is reasonable since antibody and hyaluronan layer are diluted and their refractive index is very close to that of the solvent (18). The proof of principle was realized on 10-μm diameter latex beads (IDC, sulfate-modified, smooth interface) by comparing systematically the bead movement with the predictions of the lubrication theory, in the range of distance to radius ratio $h/R \ll 1$. This was recently done similarly using TIRM measurements of diffusion parallel and orthogonal to the substrate (45). In addition, we measured, to our knowledge for the first time, the dependence of bead velocity in a flow to the instantaneous height in the range $h/R \ll 1$. Our measurements agree satisfactorily to the theory that leads to Eq. 3. This confirms experimentally the relation exploited to deduce height from velocity in flow chamber measurements (24). The second type of beads (M450; Dynal Biotech, Oslo, Norway) was more adapted to adhesion experiments: the smaller size (4.5 μm diameter) allows higher throughput and the prefunctionalization and passivation steps were realized by the supplier. However, the beads, as seen in RICM, exhibit dark and bright patches deteriorating the fringe pattern and reducing slightly the precision of the measurement. The origin of these patches, possibly surface irregularities of the bead, poses, then, further problems in defining the bead-surface distance. For this reason, we could not perform precise verification of diffusion and convection laws with these beads. However, we could still reliably estimate the thickness of the polymer, if its size exceeds the small topographical irregularities of the bead surface. One current limit of the technique is that the finite exposure time $t_{exp} = 20$ ms limits the accuracy of measurements in flow: during the recording of one frame, the displacement of a bead moving at 10 μm/s (for $G = 7\ s^{-1}$) is 0.2 μm along the flow. Therefore, the contrast of high order fringes was damped in the direction x of the flow. This affects the determination of the center position along x, but not along y direction, as checked by calculating the diffusion coefficient D_y, which is not changed by the flow. However, because the contrast damping is symmetrical in the x direction, the position of the extrema was not significantly affected for low order fringes and at low shear rates (for $G = 10\ s^{-1}$). At higher shear rate, the precise height determination will require shorter exposure time and higher frame rate, as recently achieved in experiments that track one single tethered bead (31).

Structural and physical properties of the hyaluronan layer

The thickness of the hyaluronan layers was estimated as the most probable height h^* of the beads heights distribution.

This height corresponds to the conditions of vanishing force exerted on the bead, i.e., a balance between bead weight and the electrosteric repulsion exerted by the polymer layer. Beads of both type have an effective weight $F_g = 0.235$ pN in water.

Hyaluronan molecules of molecular weight $M_w = 700{,}000$ ($N = 1700$ monomers of size $a = 1$ nm) have a persistence length $l_p = 4.2$ nm and a radius of gyration $R_g = 100$ nm (46). Assuming that all the incubating chains did bind, the average distance between the centers of adsorbed chains varies between $\xi = 55$ nm (for an incubation at [HA] = 1 μg/mL) and $\xi = 400$ nm (for [HA] = 0.02 μg/mL). One goes therefore from a configuration of isolated adsorbed chains at low HA concentration, to a sparse brush configuration at high HA concentration. The repulsive force exerted by one single chain of radius of gyration R_g at distance d is $F_{chain}(d) = 36\sqrt{3}(k_BT/R_g)\exp(-\sqrt{3}d/R_g)$ (47). This force balances the bead weight F_g at a distance $d = 140$ nm, which agrees well with the layer thickness measured at [HA] = 0.2 μg/mL (corresponding to an interchain distance $\xi = 120$ nm, at the limit between disperse and brush regime).

Some observations support the idea that the HA layer presents a certain lateral inhomogeneity at the length scale of the contact between the bead and the polymers (typically 1 μm^2): 1), the most probable height h^* increases with shear rate; 2), h^* found for M450 beads are ~10% smaller than with IDC beads; and 3), adhesion is reduced in dynamic conditions. This can be explained by the polydispersity of HA chains and by the sparse covering at low concentration. Since a single chain can repel the bead at 140 nm, a few dispersed long dangling chains can keep a bead convected by the flow far from the surface. Conversely, smaller beads can find some local depressions in the layer which are not accessible to large beads.

The apparent viscosity of the layer was estimated by fitting the dependence of the measured vertical diffusion coefficient as a function of the height. For IDC beads, which height is measured at ±5 nm, the values obtained for the viscosity are nondistinguishable from that of the solvent, at any concentration of HA. Additionally, the dependence of the velocity along the flow as a function of height follows the theoretical prediction. This is consistent with the hypothesis that the hydrodynamics is not significantly modified by the HA layer, due to the very low density of polymer. Alternatively, it can be argued the bead is too light to actually probe the viscosity of the polymer layer. Previous measurements realized with latex beads of 20-μm diameter on comparable substrates gave viscosities of ~3–4 times that of the solvent (14). More recently, relative viscosities of ~1 were measured with a dissipation quartz microbalance on brushlike HA layers (16). Interestingly, using the M450 beads, an apparent viscosity slightly higher than water at [HA] ≥ 0.2 μg/mL is measured. This raises questions about the significance of this measurement and interpretation in the case of a laterally inhomogeneous, sparse polymer layer. Expressed in terms of permeability of the hyaluronan layer, our observations are in line with the recent report that the penetration of hyaluronan layer by large solutes is controlled by the grafting density (16). Additionally, the measured velocity along the flow is smaller than the theoretical prediction (Fig. 5 *C*). A different picture would arise if one considers the possibility of a shift of the no-slip boundary condition for the fluid to the edge of the layer, as observed for a dense brush of short polymers (48).

Mechanisms of single bond formation

Among its multiple putative roles, the glycocalyx acts first as a repulsive barrier. We showed that both specific and unspecific attachments were strongly reduced by a layer of adsorbed long HA chains. As detailed in Results, two observations strongly support the fact that adhesion events correspond to single bond formation: the dilution of Fc-ICAM on the substrate leading to 1), a proportional decrease of the adhesion frequency; and 2), no measurable variation of the detachment curve (22,36). However, as in any ligand-receptor measurement technique, there is no absolute proof to test single bonds (49). The specific adhesion frequency falls by one order of magnitude when the layer exceeds 80 nm. Remarkably, the total length of the bound molecules represents four times the length of an IgG, or ~80 nm. The simultaneous fall of unspecific arrests and the above considerations about the lateral heterogeneity of the layer leads us to consider the possibility that part of the adhesion events occur in thinner parts of the polymer cushion. However, microscopic observation of fluorescently-labeled HA cushion did not reveal visible holes in the polymer layer.

The lifetime of bonds formed under different HA coating conditions were measured and reported in distributions of Fig. 6 *B*. The biphasic rupture process was not affected by the layer thickness in the range of low HA concentrations. Detachment curves obtained for higher HA concentrations are based on poorer statistics but do not exhibit any significant change compared to the no-cushion case (data not shown). This leads to the simple hypothesis that the HA layer acts to reduce the number of encounter events between the reactive partners, but the nature of the bond formed remained unchanged. An additional effect of the polymer layer could be to reduce the duration of each encounter. We performed parallel studies by varying systematically the shear rate, which is known to affect binding efficiency of cells (50). Our preliminary results indicate that the reduction of the duration of contact between molecules strongly reduces the probability of bond formation, and not in a linear manner as classically predicted (P. Robert, L. Limozin, A. Pierres, and P. Bongrand, unpublished results). In this process, the rupture kinetics was unaffected.

To distinguish between the relative effects of frequency and duration of encounter on the bond formation, one option is to perform numerical simulations. Within the framework of Pierres et al. (24), the addition of the interaction potential

induced by the polymer layer and measured here should provide insights into these mechanisms. Based on this data and using the proposed technique for further studies, the longstanding question of the role of the distance between the reactive surfaces can be now addressed quantitatively, as in recent numerical studies (51,52). As an example, we show that numerous events of close bead-substrate contact do not give rise to any detectable arrest (Fig. 7 *C*). This work represents a first step toward the measurement of the binding probability as a function of distance between the molecules and duration of encounter.

It is interesting to compare the variations of adhesion frequencies measured in dynamic conditions (Fig. 6 *A*) and the proportion of bead attached in static conditions (Fig. 6 *D*). While adhesion of the negative assay exhibits a comparable decrease as a function of hyaluronan-incubating concentration, the adhesion of the positive assay decreases faster in dynamic conditions. Half of the maximal adhesion level is reached for [HA] = 0.3 μg/mL in the static case, but for the dynamic case, it is reached at [HA] = 0.02 μg/mL. This emphasizes the relevance of operating adhesion measurements in dynamic conditions, as previously observed with cells (9,10) and raises interesting possibilities to explain these differences on a model system. For example, this is consistent with the observation that the most probable height increases systematically with shear rate.

Physiological relevance of this model

The glycocalyx has a repulsive effect on the endothelial surface, where it acts as an antiadhesive layer (53). Recent experiments have shown that endothelial glycocalyx controls leukocyte adhesion to endothelial surface (54). Inflammation induces shedding of the glycocalyx, resulting in loss of its thickness and increasing leukocyte adhesion and therefore increased leukocyte recruitment to inflamed tissues. Also, alterations of the glycocalyx in pathological circumstances could induce exaggerated leukocyte recruitment and contribute to anomalous inflammation, as seen in the initial stages of atherosclerosis (55). Understanding quantitative influence of glycocalyx on adhesion is therefore necessary to describe accurately leukocyte-endothelial interactions in physiological and pathological situations.

T lymphocyte glycocalyx is composed of several molecules including CD43, CD45, and CD148, and is much less dense than endothelial glycocalyx. Numerous T cell receptors (TCRs) are interacting with MHC-peptide complex and the half-life of these interactions is thought to be determinant in T-lymphocyte activation (56,57). Several reports indicate that the size of the TCR molecule, an MHC-peptide complex related to the size of large surface molecules around TCRs, has a direct impact on T-lymphocyte activation (58,59). An exciting hypothesis is that large extracellular domains containing molecules such as CD45 and CD148 could be expelled due to size from the vicinity of a TCR (8), as TCRs bind to MHC-peptide complex and the surfaces of a T lymphocyte and an antigen-presenting cell approach each other. Since CD45 and CD148 have intracellular phosphatase domains, balance between kinases and phosphatases would be displaced toward kinase activity around bound TCR. We demonstrated with this model that a sparse glycocalyx, as seen on the T-lymphocyte surface, has no influence on the half-life of the antigen-antibody reaction, but has a strong effect on the frequency of antigen-antibody association. The antibody-antigen interaction frequency is strongly dependent on the distance between the functionalized surfaces, and the ability to bind the ligand is dependent on the number of glycocalyx molecules, even at low surface densities. Therefore, the exploration of the modulation of adhesion by low-density glycocalyx model contributes to the understanding of the role of large surface molecules in lymphocyte activation.

CONCLUSION AND OUTLOOK

In this work, we have presented a new technique combining RICM and laminar flow chamber to study the effect of a repulsive polymer layer mimicking the glycocalyx on the formation of antigen-antibody bonds. We have found that low densities of hyaluronan can regulate the formation of bonds by reducing the number of encounter between the reaction partners. This sets the basis for further exploration of the effect of molecular environment on the bond formation of surface-attached biomolecules, through the regulation of distance and duration of reactive encounters. A promising development is the use of a supported lipid bilayer to assess the role of diffusion of the glycocalyx molecules, for example, in the context of T-cell activation.

We thank Rudolf Merkel for access to AFM for pilot measurements and Guillaume Léa for the implementation of the acquisition software.

We thank the Agence Nationale de la Recherche for financial support through grant No. JCJC06-0135.

REFERENCES

1. Robert, P., L. Limozin, A. Benoliel, A. Pierres, and P. Bongrand. 2006. Glycocalyx regulation of cell adhesion. *In* Principles of Cellular Engineering: Understanding the Biomolecular Interface. Elsevier Academic Press, Amsterdam, The Netherlands.
2. Sabri, S., M. Soler, C. Foa, A. Pierres, A. Benoliel, and P. Bongrand. 2000. Glycocalyx modulation is a physiological means of regulating cell adhesion. *J. Cell Sci.* 113:1589–1600.
3. Smith, M. L., D. S. Long, E. R. Damiano, and K. Ley. 2003. Near-wall micro-PIV reveals a hydrodynamically relevant endothelial surface layer in venules in vivo. *Biophys. J.* 85:637–645.
4. Cohen, M., E. Klein, B. Geiger, and L. Addadi. 2003. Organization and adhesive properties of the hyaluronan pericellular coat of chondrocytes and epithelial cells. *Biophys. J.* 85:1996–2005.
5. Weinbaum, S., J. M. Tarbell, and E. R. Damiano. 2007. The structure and function of the endothelial glycocalyx layer. *Annu. Rev. Biomed. Eng.* 9:121–167.

6. Stockton, B. M., G. Cheng, N. Manjunath, B. Ardman, and U. H. von Andrian. 1998. Negative regulation of T cell homing by CD43. *Immunity*. 8:373–381.
7. Wesseling, J., S. W. van der Valk, and J. Hilkens. 1996. A mechanism for inhibition of E-cadherin-mediated cell-cell adhesion by the membrane-associated mucin episialin/MUC1. *Mol. Biol. Cell*. 7:565–577.
8. Davis, S. J., and P. A. van der Merwe. 2006. The kinetic-segregation model: TCR triggering and beyond. *Nat. Immunol*. 7:803–809.
9. Sabri, S., A. Pierres, A. M. Benoliel, and P. Bongrand. 1995. Influence of surface charges on cell adhesion: difference between static and dynamic conditions. *Biochem. Cell Biol*. 73:411–420.
10. Patel, K. D., M. U. Nollert, and R. P. McEver. 1995. P-selectin must extend a sufficient length from the plasma membrane to mediate rolling of neutrophils. *J. Cell Biol*. 131:1893–1902.
11. Raviv, U., S. Giasson, N. Kampf, J.-F. Gohy, R. Jérôme, and J. Klein. 2003. Lubrication by charged polymers. *Nature*. 425:163–165.
12. Joester, D., E. Klein, B. Geiger, and L. Addadi. 2006. Temperature-sensitive micrometer-thick layers of hyaluronan grafted on microspheres. *J. Am. Chem. Soc*. 128:1119–1124.
13. Ladam, G., L. Vonna, and E. Sackmann. 2005. Protrusion force transmission of amoeboid cells crawling on soft biological tissue. *Acta Biomater*. 1:485–497.
14. Albersdorfer, A., and E. Sackmann. 1999. Swelling behavior and viscoelasticity ultrathin grafted hyaluronic acid films. *Eur. Phys. J. B*. 10:663–672.
15. Sengupta, K., J. Schilling, S. Marx, M. Fischer, A. Bacher, and E. Sackmann. 2003. Mimicking tissue surfaces by supported membrane coupled ultrathin layer of hyaluronic acid. *Langmuir*. 19:1775–1781.
16. Richter, R. P., K. K. Hock, J. Burkhartsmeyer, H. Boehm, P. Bingen, G. Wang, N. F. Steinmetz, D. J. Evans, and J. P. Spatz. 2007. Membrane-grafted hyaluronan films: a well-defined model system of glycoconjugate cell coats. *J. Am. Chem. Soc*. 129:5306–5307.
17. Boulbitch, A., Z. Guttenberg, and E. Sackmann. 2001. Kinetics of membrane adhesion mediated by ligand-receptor interaction studied with a biomimetic system. *Biophys. J*. 81:2743–2751.
18. Limozin, L., and K. Sengupta. 2007. Modulation of vesicle adhesion and spreading kinetics by hyaluronan cushions. *Biophys. J*. 93:3300–3313.
19. Evans, E. A., and D. A. Calderwood. 2007. Forces and bond dynamics in cell adhesion. *Science*. 316:1148–1153.
20. Robert, P., A.-M. Benoliel, A. Pierres, and P. Bongrand. 2007. What is the biological relevance of the specific bond properties revealed by single-molecule studies? *J. Mol. Recognit*. 20:432–447.
21. Pincet, F., and J. Husson. 2005. The solution to the streptavidin-biotin paradox: the influence of history on the strength of single molecular bonds. *Biophys. J*. 89:4374–4381.
22. Pierres, A., D. Touchard, A.-M. Benoliel, and P. Bongrand. 2002. Dissecting streptavidin-biotin interaction with a laminar flow chamber. *Biophys. J*. 82:3214–3223.
23. Pierres, A., A. M. Benoliel, P. Bongrand, and P. A. van der Merwe. 1997. The dependence of the association rate of surface-attached adhesion molecules CD2 and CD48 on separation distance. *FEBS Lett*. 403:239–244.
24. Pierres, A., A. M. Benoliel, C. Zhu, and P. Bongrand. 2001. Diffusion of microspheres in shear flow near a wall: use to measure binding rates between attached molecules. *Biophys. J*. 81:25–42.
25. Bevan, M., and D. Prieve. 2000. Hindered diffusion of colloidal particles very near to a wall: revisited. *J. Chem. Phys*. 113:1228–1236.
26. Kuhner, M., and E. Sackmann. 1996. Ultrathin hydrated dextran films grafted on glass: preparation and characterization of structural, viscous, and elastic properties by quantitative microinterferometry. *Langmuir*. 12:4866–4876.
27. Evans, E., K. Ritchie, and R. Merkel. 1995. Sensitive force technique to probe molecular adhesion and structural linkages at biological interfaces. *Biophys. J*. 68:2580–2587.
28. Stuart, J. K., and V. Hlady. 1999. Reflection interference contrast microscopy combined with scanning force microscopy verifies the nature of protein-ligand interaction force measurements. *Biophys. J*. 76:500–508.
29. Zocchi, G. 2001. Force measurements on single molecular contacts through evanescent wave microscopy. *Biophys. J*. 81:2946–2953.
30. Blumberg, S., A. Gajraj, M. W. Pennington, and J.-C. Meiners. 2005. Three-dimensional characterization of tethered microspheres by total internal reflection fluorescence microscopy. *Biophys. J*. 89:1272–1281.
31. Heinrich, V., W. Wong, K. Halvorsen, and E. Evans. 2008. Imaging biomolecular interactions by fast three-dimensional tracking of laser-confined carrier particles. *Langmuir*. 24:1194–1203.
32. Schilling, J., K. Sengupta, S. Goennenwein, A. R. Bausch, and E. Sackmann. 2004. Absolute interfacial distance measurements by dual-wavelength reflection interference contrast microscopy. *Phys. Rev. E Stat. Nonlin. Soft Matter Phys*. 69:021901.
33. McKee, C. T., S. C. Clark, J. Y. Walz, and W. A. Ducker. 2005. Relationship between scattered intensity and separation for particles in an evanescent field. *Langmuir*. 21:5783–5789.
34. Behrens, S. H., J. Plewa, and D. G. Grier. 2003. Measuring a colloidal particle's interaction with a flat surface under nonequilibrium conditions. Total internal reflection microscopy with absolute position information. *Eur. Phys. J. E Soft Matter*. 10:115–121.
35. Crocker, J. C., and D. G. Grier. 1996. Methods of digital video microscopy for colloidal studies. *J. Colloid Interface Sci*. 179:298–310.
36. Pierres, A., A. Prakasam, D. Touchard, A.-M. Benoliel, P. Bongrand, and D. Leckband. 2007. Dissecting subsecond cadherin bound states reveals an efficient way for cells to achieve ultrafast probing of their environment. *FEBS Lett*. 581:1841–1846.
37. Wild, M. K., A. Cambiaggi, M. H. Brown, E. A. Davies, H. Ohno, T. Saito, and P. A. van der Merwe. 1999. Dependence of T cell antigen recognition on the dimensions of an accessory receptor-ligand complex. *J. Exp. Med*. 190:31–41.
38. Chen, W., E. Evans, R. McEver, and C. Zhu. 2008. Monitoring receptor-ligand interactions between surfaces by thermal fluctuations. *Biophys. J*. 94:694–701.
39. Allersma, M. W., F. Gittes, M. J. deCastro, R. J. Stewart, and C. F. Schmidt. 1998. Two-dimensional tracking of NCD motility by back focal plane interferometry. *Biophys. J*. 74:1074–1085.
40. Everett, W. N., H.-J. Wu, S. G. Anekal, H.-J. Sue, and M. A. Bevan. 2007. Diffusing colloidal probes of protein and synthetic macromolecule interactions. *Biophys. J*. 92:1005–1013.
41. Hertlein, C., L. Helden, A. Gambassi, S. Dietrich, and C. Bechinger. 2008. Direct measurement of critical Casimir forces. *Nature*. 451:172–175.
42. Kleshchanok, D., and P. R. Lang. 2007. Steric repulsion by adsorbed polymer layers studied with total internal reflection microscopy. *Langmuir*. 23:4332–4339.
43. Radler, J., and E. Sackmann. 1992. On the measurement of weak repulsive and frictional colloidal forces by reflection interference contrast microscopy. *Langmuir*. 8:848–853.
44. Clack, N. G., and J. T. Groves. 2005. Many-particle tracking with nanometer resolution in three dimensions by reflection interference contrast microscopy. *Langmuir*. 21:6430–6435.
45. Huang, P., and K. S. Breuer. 2007. Direct measurement of anisotropic near-wall hindered diffusion using total internal reflection velocimetry. *Phys. Rev. E Stat. Nonlin. Soft Matter Phys*. 76:046307.
46. Takahashi, R., K. Kubota, M. Kawada, and A. Okamoto. 1999. Effect of molecular weight distribution on the solution properties of sodium hyaluronate in 0.2M NaCl solution. *Biopolymers*. 50:87–98.
47. Li, F., and F. Pincet. 2007. Confinement free energy of surfaces bearing end-grafted polymers in the mushroom regime and local measurement of the polymer density. *Langmuir*. 23:12541–12548.

48. Bevan, M., and D. Prieve. 2000. Forces and hydrodynamic interactions between polystyrene surfaces with adsorbed PEO-PPO-PEO. *Langmuir*. 16:9274–9281.

49. Zhu, C., M. Long, S. E. Chesla, and P. Bongrand. 2002. Measuring receptor/ligand interaction at the single-bond level: experimental and interpretative issues. *Ann. Biomed. Eng*. 30:305–314.

50. Rinker, K. D., V. Prabhakar, and G. A. Truskey. 2001. Effect of contact time and force on monocyte adhesion to vascular endothelium. *Biophys. J*. 80:1722–1732.

51. Korn, C. B., and U. S. Schwarz. 2007. Mean first passage times for bond formation for a Brownian particle in linear shear flow above a wall. *J. Chem. Phys*. 126:095103.

52. Mody, N. A., and M. R. King. 2007. Influence of Brownian motion on blood platelet flow behavior and adhesive dynamics near a planar wall. *Langmuir*. 23:6321–6328.

53. Frey, A., K. T. Giannasca, R. Weltzin, P. J. Giannasca, H. Reggio, W. I. Lencer, and M. R. Neutra. 1996. Role of the glycocalyx in regulating access of microparticles to apical plasma membranes of intestinal epithelial cells: implications for microbial attachment and oral vaccine targeting. *J. Exp. Med*. 184:1045–1059.

54. Mulivor, A. W., and H. H. Lipowsky. 2004. Inflammation- and ischemia-induced shedding of venular glycocalyx. *Am. J. Physiol. Heart Circ. Physiol*. 286:H1672–H1680.

55. Constantinescu, A. A., H. Vink, and J. A. E. Spaan. 2003. Endothelial cell glycocalyx modulates immobilization of leukocytes at the endothelial surface. *Arterioscler. Thromb. Vasc. Biol*. 23:1541–1547.

56. Matsui, K., J. J. Boniface, P. Steffner, P. A. Reay, and M. M. Davis. 1994. Kinetics of T-cell receptor binding to peptide/I-Ek complexes: correlation of the dissociation rate with T-cell responsiveness. *Proc. Natl. Acad. Sci. USA*. 91:12862–12866.

57. Carreño, L. J., S. M. Bueno, P. Bull, S. G. Nathenson, and A. M. Kalergis. 2007. The half-life of the T-cell receptor/peptide-major histocompatibility complex interaction can modulate T-cell activation in response to bacterial challenge. *Immunology*. 121:227–237.

58. Irles, C., A. Symons, F. Michel, T. R. Bakker, P. A. van der Merwe, and O. Acuto. 2003. CD45 ectodomain controls interaction with GEMs and Lck activity for optimal TCR signaling. *Nat. Immunol*. 4:189–197.

59. Choudhuri, K., D. Wiseman, M. H. Brown, K. Gould, and P. A. van der Merwe. 2005. T-cell receptor triggering is critically dependent on the dimensions of its peptide-MHC ligand. *Nature*. 436:578–582.